infrastructures

MDPI

Article

Investigation of the Influence of Spoiler and Maintenance Track on Second-Order Heaving Vortex-Induced Vibration

Feng Wang [1], Jiqing Luo [2], Shuohua Xu [2], Peisen Li [2], Jiamin Dang [3], Guangzhong Gao [1], Jiaying Wang [1,*] and Haodao Li [3]

[1] School of Highway, Chang'an University, Xi'an 710064, China; wf@chd.edu.cn (F.W.); ggz@chd.edu.cn (G.G.)
[2] Guangdong Provincial Highway Construction Co., Ltd., Guangzhou 510030, China
[3] Civil, Architectural and Environmental Engineering, Missouri University of Science and Technology, Rolla, MO 65409, USA; jdtbk@mst.edu (J.D.); hlbb4@mst.edu (H.L.)
* Correspondence: wjying@chd.edu.cn

Abstract: To improve the guidance for the wind tunnel test, this study initially conducted thorough research on the wind environment at a coastal bridge site to ascertain the characteristics of the wind parameters varying along the bridge span. Subsequently, the measured results were utilized to steer wind tunnel test research, focusing on analyzing the influence of the spoiler and maintenance track on the second-order heaving vortex-induced vibration of the flat steel box girder. This investigation uncovered two distinct distributions in the angle of attack along the span: bimodal distribution and asymmetric unimodal distribution. The angle of attack of the incoming flow was primarily concentrated within ±5°. Both the two-side and the windward spoiler were found to exert similar effects on the second-order heaving vortex-induced vibration, primarily impacting the second lock-in region. Furthermore, the outer maintenance track could effectively suppress the vortex-induced vibration, while the spacing of the inner maintenance track significantly affected the vortex-induced vibration at high wind speeds.

Keywords: field measurement; wind tunnel test; spoiler; maintenance track; second-order heaving vortex-induced vibration

Citation: Wang, F.; Luo, J.; Xu, S.; Li, P.; Dang, J.; Gao, G.; Wang, J.; Li, H. Investigation of the Influence of Spoiler and Maintenance Track on Second-Order Heaving Vortex-Induced Vibration. *Infrastructures* **2024**, *9*, 192. https://doi.org/10.3390/infrastructures9110192

Academic Editor: Tatiana García-Segura

Received: 13 September 2024
Revised: 6 October 2024
Accepted: 25 October 2024
Published: 28 October 2024

1. Introduction

The flat steel box girder, a common section form of long-span bridges, is susceptible to vortex-induced vibration due to its tendency to detach and reattach when subjected to airflow. Vortex-induced vibration is a prevalent wind-induced vibration phenomenon occurring at low wind speeds. Its frequent incidence can diminish driving comfort and precipitate bridge fatigue. Consequently, the control of vortex-induced vibration has emerged as a key research focus.

Typically, vortex-induced vibration is closely correlated with incoming flow conditions. Various factors such as the incoming wind speed, angle of attack, and wind direction substantially influence the characteristics of vortex-induced vibration. Consequently, numerous researchers have conducted extensive studies on the wind environment at bridge sites in order to delve deeper into this phenomenon. For instance, Zhang et al. (2023) conducted an analysis of the wind speed, wind direction, and angle of attack at a bridge site during typhoon conditions [1]. Hui et al. (2009) delved into the mean and fluctuating wind characteristics around Stonecutters Bridge through field measurements [2], while Li et al. (2017) examined the flow characteristics within a wind field using field measurements [3]. Fenerci et al. (2017) performed field measurements at the Hardanger Bridge and examined the wind environment and structural response at the bridge site [4]. Wu et al. (2023) investigated the wind environment near a bridge floor in a deep canyon landform through field measurements [5]. Additionally, Vickery and Twisdale (1995) integrated field measurements with a theoretical analysis to develop a sophisticated typhoon wind field

model [6]. While numerous studies have focused on the wind environment at bridge sites, few scholars have utilized the measured wind environment results to direct wind tunnel tests in engineering practice. This has resulted in discrepancies between wind tunnel test outcomes and actual conditions. Consequently, optimizing the use of measured wind environment results to guide wind tunnel tests has emerged as another research focal point.

In the investigation of vortex-induced vibration in bridges, research methods such as wind tunnel tests, numerical simulations, and field measurements are commonly employed, with many scholars utilizing these methods to study bridges with various section forms (Bai et al., 2021 [7]; Wang et al., 2024 [8]; Zhang et al., 2020 [9]). For instance, Wu et al. (2022) took a cable-stayed bridge without backstays as a research object. They adopted 0° and ±3° angles to evaluate the wind-induced vibration performances during the research [10]. Li et al. (2024) conducted wind tunnel tests to study the aerodynamic interference between vehicles and a girder at 0° and ±3° [11]. Larsen et al. (2000) conducted a wind tunnel test to examine the impact of railings and guide vanes on the vortex-induced vibration of flat steel box girders. The test results indicated that the guide vanes could enhance the section's vortex-induced vibration performance, while the effect of the railings was found to be the opposite [12]. Additionally, Laima et al. (2018) and Yuan et al. (2017) individually studied the causes of the lock-in region of a twin box girder using the PIV method at 0° [13,14]. Huang et al. (2022) conducted wind tunnel tests and numerical simulations to investigate the impact of horizontal guide vanes on sections with varying aspect ratios at 0°, ±3°, and ±5° [15]. Their findings suggested that the effect of the horizontal guide vanes varied depending on the location and installation object. Wang et al. (2024) explored the characteristics of the vortex-induced vibration of a 5:1 rectangular section through numerical simulations, revealing the presence of two distinct vortex-induced vibration forms: "resonance-induced" and "competition-induced" [16]. Li et al. (2022) combined a wind tunnel test and numerical simulation to explore the influence of the guide vanes on a two-lock-in region at 0° [17]. Furthermore, for spoilers, Zhao et al. (2022) utilized a field measurement method to monitor the vortex-induced vibration that occurred on Humen Bridge, and the installed spoiler suppressed the amplitude [18]. Hu et al. (2024) used the wind tunnel test to study the mechanism of the first-order vortex-induced vibration of a typical streamlined closed-box girder and found that spoilers can suppress vortex formation to suppress vibration at 0° [19]. Xu et al. (2016) conducted a vibration–pressure test and found the installation of a spoiler affects the surface pressure distribution so as to affect the aerodynamic performance at 0°, ±3°, and ±5° [20]. For maintenance tracks, Chen et al. (2020) found the position of maintenance tracks could improve first-order vortex-induced vibration performance at 0°, ±3°, ±5°, and −10° [21]. Yang et al. (2021) took a split three-box girder bridge as an objective and found a vortex would form behind the maintenance tracks at 0° and ±3° [22]. Ge et al. (2022) utilized field measurements, the wind tunnel test, and numerical simulation to investigate the vortex-induced vibration of Humen Bridge at 0°, ±3°, and ±5° and found that the use of a maintenance rail was a key measure to suppress the vibration [23]. Li et al. (2018) adopted the wind tunnel test to investigate the vortex-induced vibration optimization of a wide streamlined box girder at 0°, ±3°, and ±5°; they also found the use of a maintenance track was a measure to suppress the vibration [24]. To sum up, most existing studies have studied the vortex-induced vibration of various sections based on the first-order heaving frequency, while few scholars have studied the vibration suppression of high-order vortex-induced vibration. However, in reality, high-order vortex-induced vibration often occurs at low wind speeds. This phenomenon indicates that the study of first-order vortex-induced vibration is likely to lead to some deviation between the actual phenomenon and the experimental results. On the other hand, the selection of the angle of attack in the existing studies is relatively broad. Different scholars have their own research habits [25,26]. Generally, researchers believe that a ±3° angle of attack more frequently occurs in the actual situation, and most researchers tend to focus on this scope to conduct research. It is easy for designers or other researchers to overestimate vortex-induced vibration performance.

Therefore, three ultrasonic anemometers were installed at the bridge site to acquire the actual inflow angle of attack, wind speed, and other characteristics. Subsequently, based on the measured wind angle of attack, wind tunnel tests were conducted to assess the vortex-induced vibration with the second-order heaving frequency of the bridge. This research focuses on examining the impact of different spoiler sizes and access paths on the second-order vortex-induced vibration under varying angles of attack.

2. Field Measurement

2.1. Measured Site and Equipment Layout

In this paper, we analyze the characteristics of wind fields around a bridge situated on the southeast coast of China. The measured site-owned characteristics were an estuary with a flat terrain and an open water surface. Given this, the terrain roughness could be regarded as smooth. During the field measurement process, three observation points, including a mid-point and two quarter-points, were positioned along the span direction at the height of the bridge pavement, as depicted in Figure 1. To better consider the influence of the normal wind, in the subsequent data processing, the data on typhoon days were eliminated.

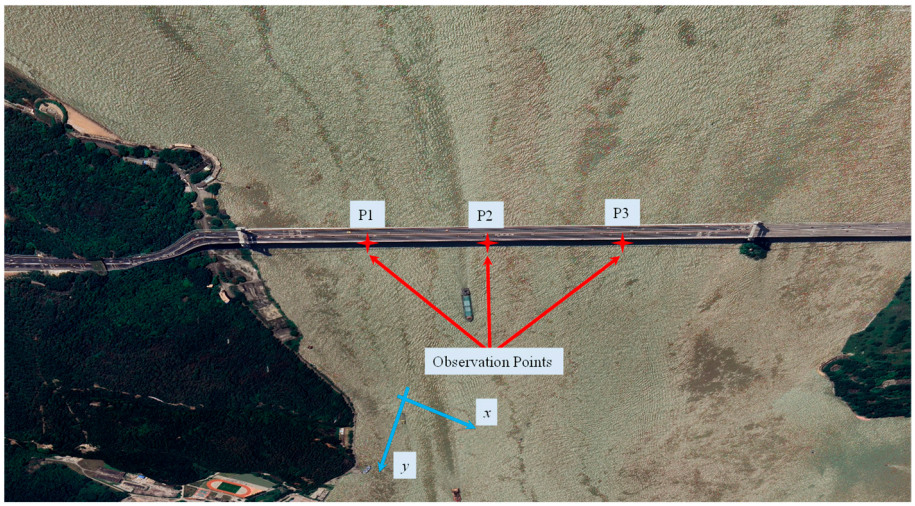

Figure 1. Layout of measured points.

The ultrasonic anemometer model 81,000 was utilized to capture real-time data on the wind speed and direction. The sampling frequency was configured at 4 Hz, with due north designated as 0° and due east as 90°. The *Y*-axis corresponds to the north–south direction, while the *X*-axis represents the east–west direction. Regarding wind speed, the device's monitoring range spans from 0 to 40 m/s, with a resolution of 0.01 m/s and a threshold of 0.01 m/s. In the wind speed range of 0–30 m/s, the accuracy stands at ±1% RMS ± 0.05 m/s, and in the range of 30–40 m/s, the accuracy is ±3% RMS. In terms of wind direction, the device monitors an azimuth range of 0 to 359.9 degrees, an elevation range of ±60.0 degrees, and operates with a resolution of 0.1 degrees. When monitoring the wind speed within the 0–30 m/s range, the wind direction accuracy is ±2°, and within the 30–40 m/s range, the accuracy is ±5°. The installation diagram of the equipment is illustrated in Figure 2.

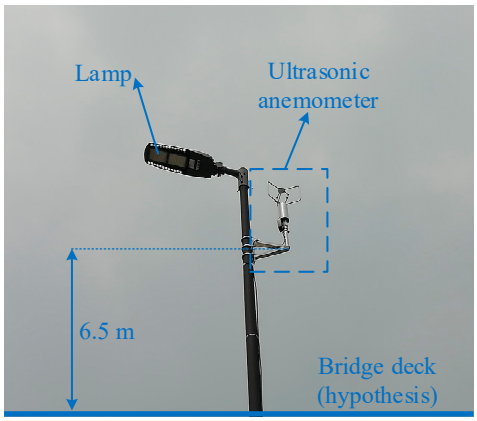

Figure 2. The installation diagram of the ultrasonic anemometer.

2.2. Field Measurement Data Processing

The measured wind speed and angle of attack were utilized to facilitate the subsequent wind tunnel test. During the analysis of the measured wind speed, Equation (1) was pertinent for calculating the mean wind speed, while Equation (2) was employed for determining the mean angle of attack.

$$\begin{cases} u_x = -u \sin \alpha \\ u_y = -u \cos \alpha \\ U = \sqrt{\overline{u}^2{}_x + \overline{u}^2{}_y} \end{cases} \tag{1}$$

where u, u_x, and u_y represent the incoming wind speed and the component of wind speed on the x and y axis, respectively. U, $\overline{u}_x$, and $\overline{u}_y$ denote the 10-min mean wind speed in the incoming, x, or y directions, respectively. α represents the incoming wind direction.

$$\theta = \arctan(\frac{\overline{u}_z}{U}) \tag{2}$$

where $\overline{u}_z$ denotes the 10-min vertical mean wind speed, and θ represents the angle of attack.

2.3. Measured Results

The data presented in Figure 3 illustrate the prevailing wind directions observed at each monitoring point. The figure depicts a predominant southeastern wind pattern, although it deviates from a normal distribution and demonstrates inconsistency in the wind direction distribution of each monitoring point. At monitoring point P1, the incoming wind is primarily concentrated between 59° and 82° and 140° and 175°. Conversely, at monitoring point P2, the predominant wind direction lies between 151° and 198°. Monitoring point P3 registers an influx of wind primarily between 128° and 186°. These findings indicate non-uniform spatial flow conditions, suggesting the presence of complex three-dimensional flow characteristics around the bridge section.

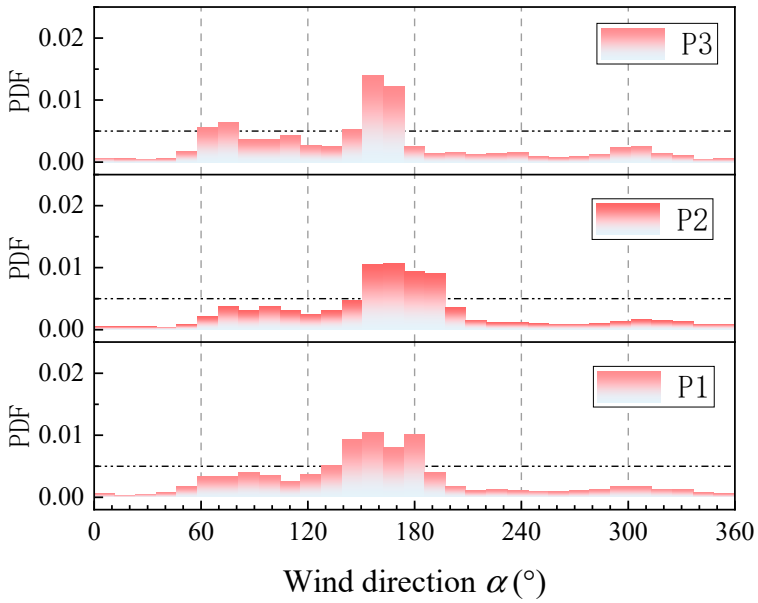

Figure 3. Wind direction distribution at different monitoring points.

In Figure 4, the distribution characteristics of the mean wind speed and mean angle of attack at the bridge site are presented. A kernel smooth distribution is applied to fit the data when analyzing the characteristics of the wind speed and angle of attack. In Figure 4a, the wind speed distribution at the quarter point displays a conspicuous bimodal pattern, with most wind speeds falling below 10 m/s. Meanwhile, the distribution of the angles of attack exhibits a subtle bimodal pattern, with the majority of angles ranging between $-5°$ and $5°$ and a smaller portion ranging from $5°$ to $10°$. In Figure 4b, the second peak interval of the angle of attack exhibits an enhanced prominence, displaying a clear bimodal distribution. The first peak interval falls between $-5°$ and $5°$, while the second peak ranges from $5°$ to $10°$. Although the bimodal distribution of the wind speed shows a slight degradation, an overall bimodal distribution is evident, with the mean wind speed predominantly concentrated below 10 m/s. In Figure 4c, the distribution of the angles of attack transition from a bimodal distribution to a unimodal distribution, with the angles of attack primarily concentrated between $-5°$ and $5°$. Additionally, the wind speed distribution experiences further degradation to a unimodal distribution, with the majority of the mean wind speeds falling within 10 m/s. In conjunction with the findings presented in Figure 4, it is apparent that the wind speed and angles of attack demonstrate distinct spatially non-uniform distributions along the span direction. The different bridge locations within the comparable wind speed ranges exhibit two distinct forms of incoming wind speed distribution: asymmetric unimodal distribution and bimodal distribution. In the distribution characteristics of the angles of attack, it is observed that the angles of attack also exhibit a distribution pattern akin to the wind speed. The angle of attack between the incoming wind and the cross-section predominantly falls within the range of $-5°$ to $5°$. This observation suggests that a $\pm 3°$ angle of attack, employed in wind tunnel tests for bridge construction, is more reasonable. Although studying the spatially non-uniform angle of attack poses challenges in wind tunnel testing, it is essential to ensure that the selected test angles of attack cover the actual range of the angles of attack and account for the influence of significant angles of attack. Based on the statistical characteristics measured, wind tunnel tests will be conducted to investigate the second-order vortex-induced vibration performance of the flat steel box beams within the angles of attack of $-5°$ to $5°$.

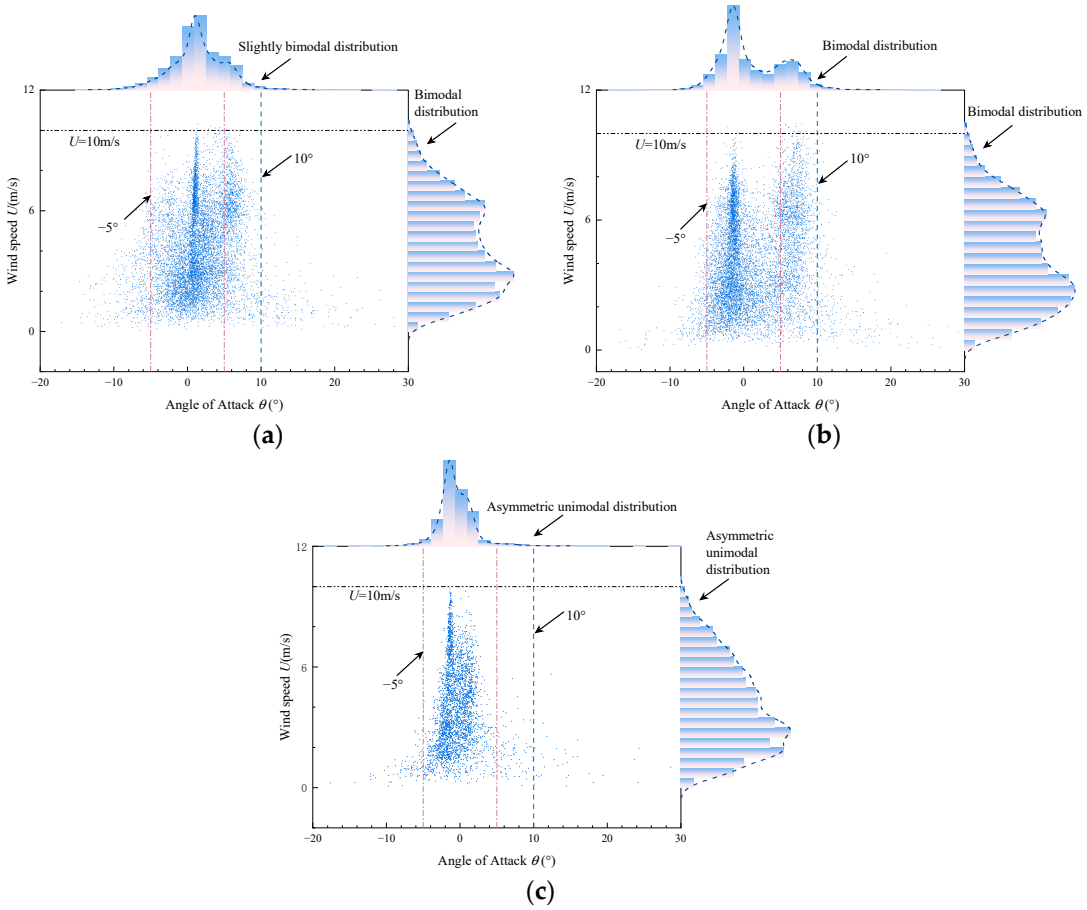

Figure 4. Distribution of mean wind speed and mean angle of attack. (**a**) P1; (**b**) P2; (**c**) P3.

3. Wind Tunnel Tests

3.1. Wind Tunnel Experiment Setup

To utilize the recorded wind field data in guiding the wind tunnel experiments, this study performed wind tunnel tests on the bridge, specifically focusing on investigating the second-order heaving vortex-induced vibration characteristic. The primary objective was to identify effective aerodynamic measurements for suppressing vibration. The selected bridge for the assessment was a suspension cable system with an 888 m main span and a main cable sag-to-span ratio of 1:10.5. The bridge section featured a streamlined closed steel box girder with a section width of 35.6 m, a beam height of 3.012 m, and a width-to-height ratio of 1/11.82, as depicted in Figure 5. The spoiler was not installed in the original case, but the outer and inner maintenance tracks were installed. The experiments were conducted at the wind tunnel of Chang'an University; the wind tunnel owns a test section with a length of 15 m, width of 3 m, and height of 2.5 m, and the test turbulence is less than 0.5%.

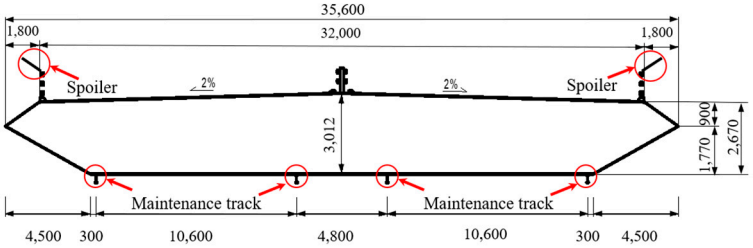

Figure 5. Cross-section of the main beam (unit: mm).

In the testing process, the model's geometric scaling ratio was 1:60, with the model measuring 1.8 m in length, 0.593 m in width (b), and 0.0502 m in height (h), resulting in an aspect ratio (l/b) of 3.04. The motion characteristics were simulated using eight linear elastic springs. To minimize the impact of the end effect, an oval end plate was installed. The displacement of the section was monitored using a PSI laser displacement meter with a sampling frequency set to 800 Hz. The laser displacement meter adopts diffuse reflection as the measurement method; the resolution is 20 μm. The wind tunnel test model is illustrated in Figure 6. In bridge wind engineering, vortex-induced vibration is influenced by aerodynamic shape, so the model's stiffness was supported by an aluminum frame, and the outer part was made of wood to ensure the model's mass did not exceed the target mass. The auxiliary facilities, such as the railing and maintenance tracks, were made of plastic. The primary motion parameters of the model are detailed in Table 1.

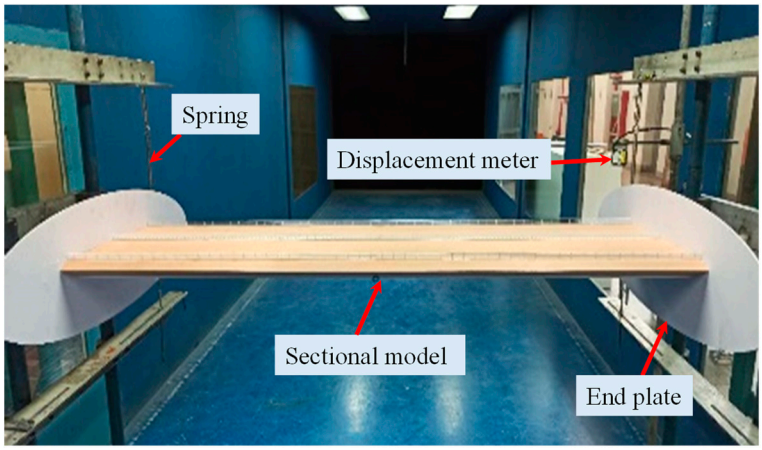

Figure 6. The layout of the wind tunnel test.

Table 1. Motion parameters of wind tunnel test model.

Mode	Actual Situation			Model			
	Frequency (Hz)	Mass per Unit ($kg \cdot m^{-1}$)	Geometric Scale Ratio	Frequency (Hz)	Damping Ratio (%)	Mass per Unit ($kg \cdot m^{-1}$)	Wind Speed Ratio
Second-order asymmetric heave	0.277	23,765.8	1:60	5.53	0.26	6.77	1:3.24

3.2. Experimental Data Processing

When the wind tunnel testing was utilized to investigate the second-order heaving vortex-induced vibration performance at the various angles of attack, Equation (3) was employed to analyze the gathered data and determine the dimensionless displacement value. The equation references the literature in [27].

$$A_h = \frac{\sqrt{2} \times RMS(A)}{D} \times \frac{2\sqrt{3}}{3} \times n \quad (3)$$

where A_h symbolizes the heaving dimensionless amplitude, A represents the amplitude, D denotes the sectional height, and n signifies the geometrical scale ratio.

4. Discussion

4.1. The Influence of Spoiler on Original Section

Figure 7a illustrates the second-order heaving vortex-induced vibration performance of the flat steel box beam at the various angles of attack. A lock-in region is evident at low

wind speeds. Notably, when the angle of attack is +5°, a second lock-in region emerges at high wind speeds. Figure 7b shows the variation in the maximum amplitude and the length of the lock-in region with the angle of attack. As can be seen from the figure, as the angle of attack changes from positive to negative, the maximum amplitude of the first lock-in region gradually increases. However, there is no obvious rule that the length of the lock-in region varies with the angle of attack. The length of the lock-in region is at its maximum at 0° and at its minimum at −5°. When the second lock-in region is present, the maximum amplitude of the first lock-in region is significantly greater than the maximum amplitude of the second lock-in region, but the length of the two locking regions is equal. The phenomenon depicted in Figure 7 suggests that the second-order heaving vortex-induced vibration performance may degrade with the increase in the angle of attack. Furthermore, this observation highlights the importance of considering the impact of large angles of attack when conducting wind tunnel tests.

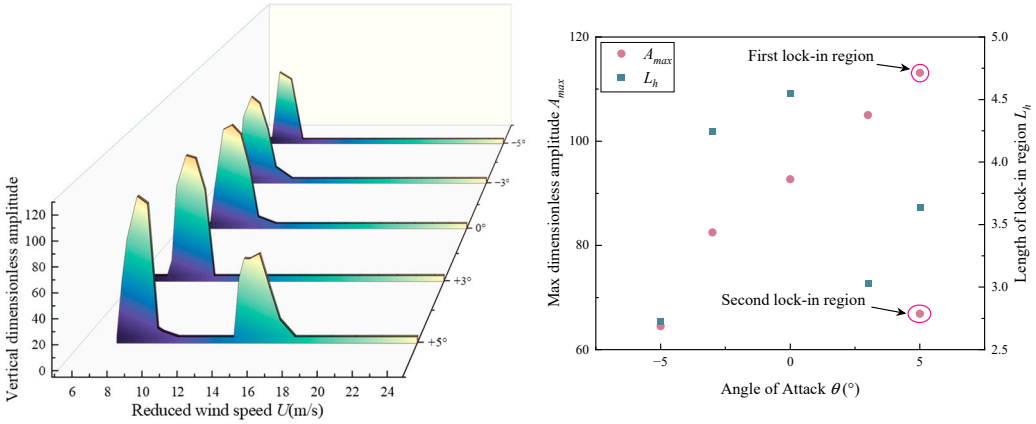

(**a**) (**b**)

Figure 7. Vibration characteristics of the original section at different angles of attack. (**a**) The amplitude varies with the wind speed; (**b**) the maximum amplitude and lock-in region vary with the angle of attack.

4.2. The Influence of Spoiler Size and Form

To mitigate the second-order heaving vortex-induced vibration of the original section, the influence of spoilers of various sizes was examined in this study. Throughout the experiment, the spoiler was positioned at a 45° angle to the horizontal plane, as illustrated in Figure 5.

Figure 8 shows the second-order heaving vortex-induced vibration performance under the action of a 30 cm spoiler (converted to actual size). As can be seen from Figure 8a, when the angle of attack is +5°, the second lock-in region disappears. There is only one lock-in region for the various angles of attack. In Figure 8b, −5° has the maximum heaving amplitude and the shortest length of the lock-in region, while the maximum heaving amplitude and the length of the lock-in region are close to each other at the other angles of attack. Compared to Figure 7b, only the maximum amplitude of −5° increases slightly, while the amplitudes of the other angles of attack decrease significantly. In addition, the length of the lock-in region is also shortened on the whole.

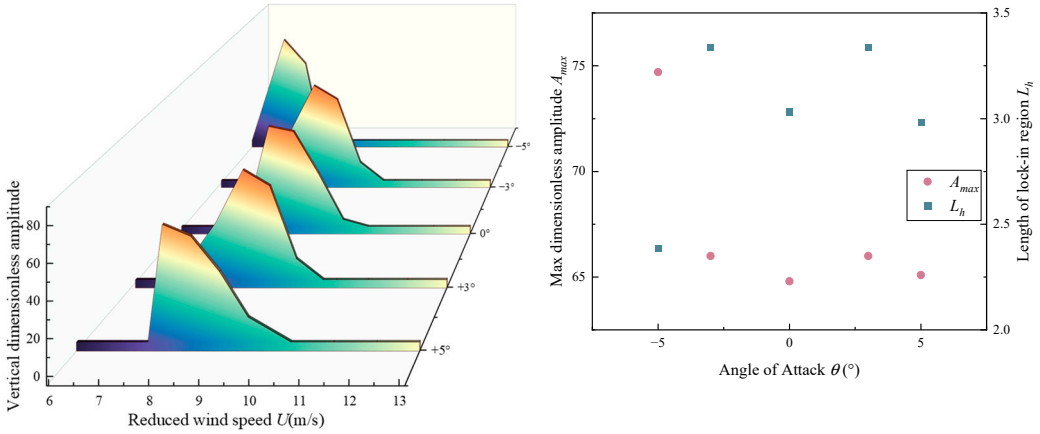

Figure 8. Influence of the bilateral 30 cm spoiler. (**a**) The amplitude varies with the wind speed; (**b**) the maximum amplitude and lock-in region vary with the angle of attack.

Figure 9 illustrates the second-order heaving vortex-induced vibration performance under the influence of a 45 cm spoiler. Upon increasing the length of the spoiler from 30 cm to 45 cm, the flat steel box girder exhibits a low wind speed lock-in region at each angle of attack, with an additional high wind speed lock-in region introduced at $-5°$. This observation suggests that the size of the spoiler impacts the emergence of the second lock-in region. In Figure 9b, the maximum amplitude of the first lock-in region transitions from negative to positive with the angle of attack, differing from the pattern seen in Figure 8b, wherein it initially decreases and then increases. Furthermore, at $-5°$, the length of the second lock-in region is notably greater than that of the first lock-in region; however, its maximum amplitude is smaller than that of the first lock-in region. This occurrence further underscores that the spoiler's size influences the second lock-in region's appearance at a large attack angle.

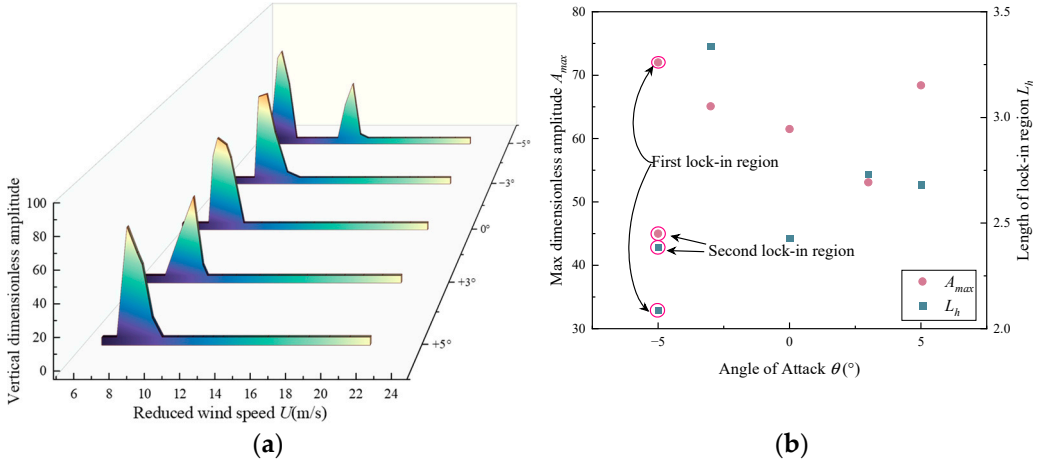

Figure 9. Influence of the bilateral 45 cm spoiler. (**a**) The amplitude varies with the wind speed; (**b**) the maximum amplitude and lock-in region vary with the angle of attack.

Figure 10 further shows the second-order heaving vortex-induced vibration performance with the increase in the spoiler size. When the spoiler size increases from 45 cm to 50 cm, a second lock-in region appears at $\pm 5°$. When the angle of attack is $-5°$, the maximum amplitude of the second lock-in region is greater than the maximum amplitude of that at +5°. In addition, according to Figure 10b, when the second lock-in region appears, the length of the second lock-in region is smaller than the length of the first lock-in region, but the maximum amplitude of the second lock-in region is smaller than the maximum

amplitude of the first lock-in region. In combination with Figure 9b, the size of the spoiler affects the length of the second lock-in region and its maximum amplitude.

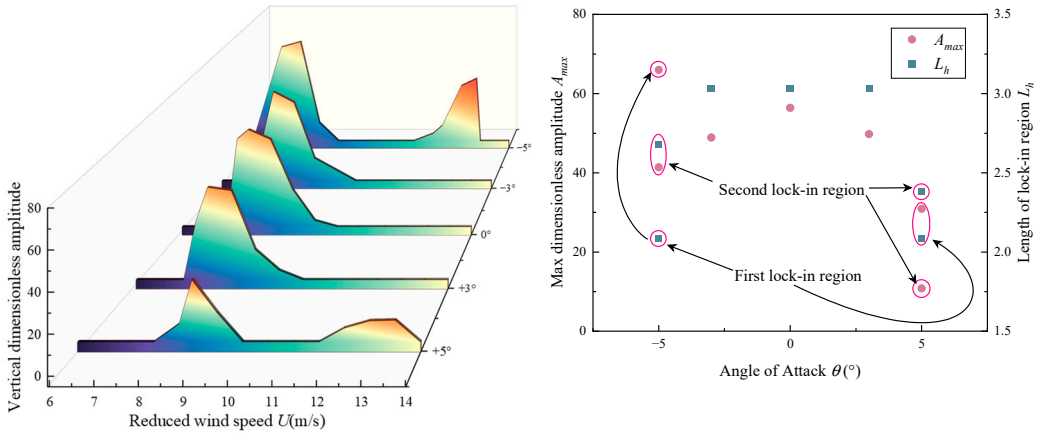

(**a**) (**b**)

Figure 10. Influence of the bilateral 50 cm spoiler. (**a**) The amplitude varies with the wind speed; (**b**) the maximum amplitude and lock-in region vary with the angle of attack.

Upon the aforementioned study, it becomes apparent that the bilateral spoilers exert a substantial influence on the second-order heaving vortex-induced vibration performance. Furthermore, the function of the spoiler is examined by instituting a "unilateral 45 cm spoiler". Analysis of Figure 11 reveals a marginal increase in amplitude at a −5° angle, whereas the maximum amplitude at other angles of attack appears to decline. Moreover, a slight decrease was observed in the length of the lock-in region. A comparative examination of Figures 9 and 11 illustrates a resemblance in the impact of the windward side and bilateral spoiler on the second-order heaving vortex-induced vi-bration.

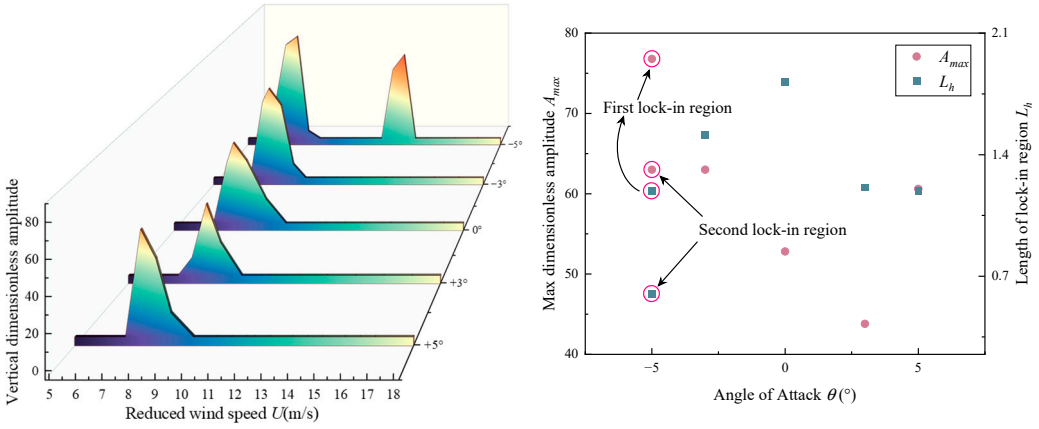

(**a**) (**b**)

Figure 11. Influence of the 45 cm spoiler of the windward site. (**a**) The amplitude varies with the wind speed; (**b**) the maximum amplitude and lock-in region vary with the angle of attack.

4.3. The Influence of Maintenance Track

The aerodynamic shape of long-span bridges significantly influences the wind-induced vibration performance. Despite the relatively small size of the maintenance track in relation to the overall section, an unreasonable arrangement may lead to a deterioration in the wind-induced vibration performance. In this study, the impact of removing the outer maintenance track on the wind-induced vibration performance was first investigated, followed by the adjustment of the spacing of the inner maintenance track from 8 cm to 16 cm. Figure 12 illustrates the second-order heaving vortex performance when the outer

maintenance track is removed. The removal of the outer maintenance track results in a significant improvement in the vortex-induced vibration performance under the various angles of attack, even with the existence of a two-lock-in region at +5°. Combining this observation with the phenomenon shown in Figure 7, the outer maintenance track notably influences the low wind speed's vortex-induced vibration performance under a negative angle of attack.

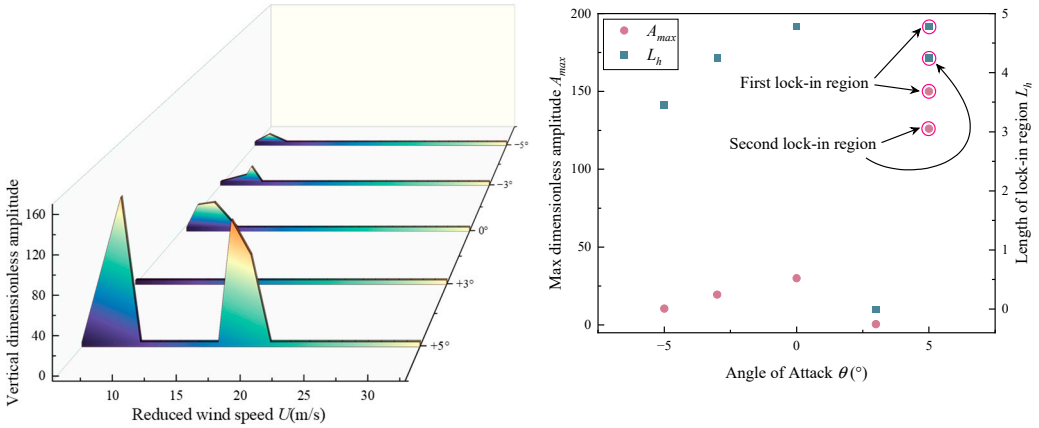

Figure 12. Vortex-induced vibration performance without the outer maintenance track. (**a**) The amplitude varies with the wind speed; (**b**) the maximum amplitude and lock-in region vary with the angle of attack.

The observation depicted in Figure 12 highlights the significant impact of the outer maintenance track's presence or absence on the second-order vortex-induced vibration. To further explore the influence of the maintenance track on the second-order vortex-induced vibration, this study examines the impact of the inner maintenance track on the second-order vortex-induced vibration performance by adjusting the spacing from 8 cm to 16 cm. As illustrated in Figure 13, a lock-in region is solely evident at +5°, with the vortex-induced vibration phenomena at the other angles of attack being eliminated. Compared to the phenomenon shown in Figure 12, although a lock-in region at high wind speeds remains present, its maximum amplitude decreases significantly. This observation indicates that the arrangement of the inner maintenance track can effectively regulate the lock-in region at low wind speeds, emphasizing the substantial influence of the maintenance track arrangement on the second-order vortex-induced vibration performance.

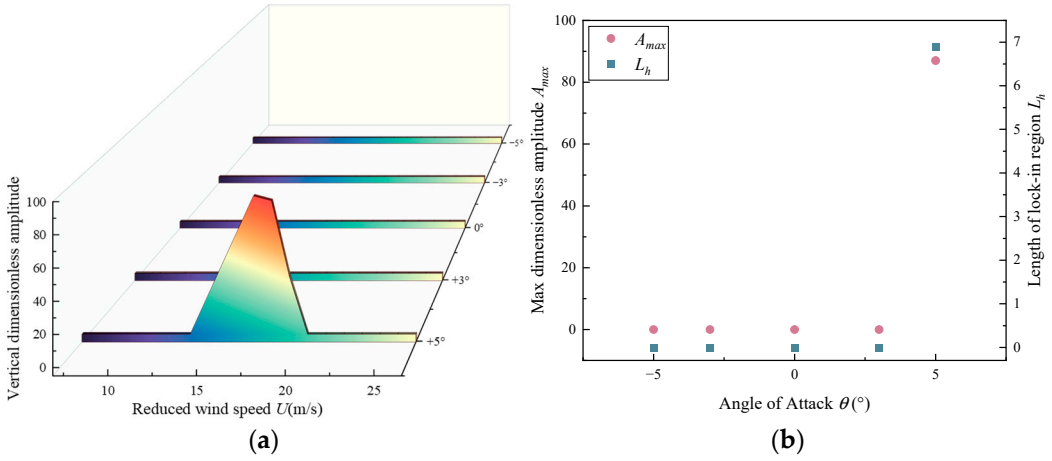

Figure 13. The influence of the inner maintenance track. (**a**) The amplitude varies with the wind speed; (**b**) the maximum amplitude and lock-in region vary with the angle of attack.

5. Conclusions

The paper presents an analysis of the wind speed and angles of attack at the various positions of long-span suspension bridges obtained through field measurements. These data were utilized to guide the wind tunnel tests investigating the second-order heaving vortex-induced vibration characteristics of long-span suspension bridges with a sag-to-span ratio of 1:10.5 and a width–height ratio of 11.82 at different angles of attack. Furthermore, the impact of the spoilers and maintenance tracks on the second-order heaving vortex-induced vibration was also examined. The conclusions are as follows:

There were obvious three-dimensional flow characteristics around the long-span suspension bridge at the estuary. There were two different distributions of the wind direction and angle of attack at different positions along the span: bimodal distribution and unimodal distribution. The angle of attack near the estuary was mainly between -5° and $+5^\circ$, and a small part was between $+5^\circ$ and $+10^\circ$. In the wind tunnel test, the second-order heaving vortex-induced vibration at $\pm5^\circ$ was more unfavorable than that at $\pm3^\circ$, and the second lock-in region occurred at -5°. When the wind tunnel tests were conducted, the $\pm5^\circ$ angles of attack were suggested to avoid overestimating the vortex-induced vibration performance.

The size of the spoiler affected the second-order heaving vortex-induced vibration performance of the flat steel box girder by influencing the second lock-in region. When the spoiler was 30 cm, the second lock-in region was first suppressed; when the spoiler size was 45 cm, the second lock-in region occurred at $+5^\circ$, and the influence of the two-sided layout was similar to that of the windward layout; when the spoiler was 50 cm, the vortex-induced vibration performance deteriorated, and the second lock-in region occurred at $\pm5^\circ$. Therefore, a spoiler with a 45° inclined angle and 30 cm length is suggested.

The presence of the outer maintenance track reduced the second-order heaving vortex-induced vibration performance at the negative attack angles, 0°, and $+3^\circ$. However, the inner maintenance track spacing significantly affected the second-order heaving vortex-induced vibration performance at low wind speeds. When the size reached 16 cm, the low wind speed lock-in region of each angle of attack was eliminated. An outer maintenance track is not suggested, and an inner maintenance track with a spacing of 16 cm (actual situation 9.6 m) is suggested.

Author Contributions: Software, F.W. and J.L.; formal analysis, J.W., F.W. and S.X.; writing—original draft, F.W. and J.L.; writing—review and editing, J.W., J.D. and H.L.; project administration, J.W. and F.W.; conceptualization, F.W. and P.L.; methodology, J.D., G.G., S.X., P.L. and H.L.; funding acquisition, G.G. All authors have read and agreed to the published version of the manuscript.

Funding: The work was funded by the Research Funds for the Interdisciplinary Projects, CHU (Grant No. 300104240923).

Data Availability Statement: The data that support the findings of this study are available from the corresponding author upon reasonable request.

Acknowledgments: The help provided by the Wind Tunnel Laboratory of Chang'an University is gratefully acknowledged.

Conflicts of Interest: Jiqing Luo, Shuohua Xu and Peisen Li are employed by Guangdong Provincial Highway Construction Co., Ltd. The authors declare that they have no known competing financial interests or personal relationships that could have appeared to influence the work reported in this paper.

References

1. Zhang, H.; Wang, H.; Xu, Z.; Tao, T.; Mao, J.; Gao, H. Measurement study on wind characteristics model at bridge site considering typhoon spatial position. *J. Vib. Eng.* **2023**, *36*, 1430–1436.
2. Hui, M.; Larsen, A.; Xiang, H.F. Wind turbulence characteristics study at the stonecutters bridge site: Part II: Wind power spectra, integral length scales and coherences. *J. Wind Eng. Ind. Aerodyn.* **2009**, *97*, 48–59. [CrossRef]
3. Li, Y.; Hu, P.; Xu, X.; Qiu, J. Wind characteristics at bridge site in a deep-cutting gorge by wind tunnel test. *J. Wind Eng. Ind. Aerodyn.* **2017**, *160*, 30–46. [CrossRef]

4. Fenerci, A.; Ole, O.; Anders, R. Long-term monitoring of wind field characteristics and dynamic response of along-span suspension bridge in complex terrain. *Eng. Struct.* **2017**, *147*, 269–284. [CrossRef]
5. Wu, F.; Cui, W.; Zhao, L.; Guo, Z.; Li, Q.; Ge, Y. Field Measurements of Wind Microclimate for Vehicle Levels on a Bridge Deck in a Complex Deep Canyon Terrain. *China J. Highw. Transp.* **2023**, *36*, 71–81.
6. Vickery, P.J.; Twisdale, L.A. Wind-field and filling models for hurricane wind-speed predictions. *J. Struct. Eng.* **1995**, *121*, 1700–1709. [CrossRef]
7. Bai, H.; Li, R.; Xu, G.; Kareem, A. Aerodynamic performance of Π-shaped composite deck cable-stayed bridges including VIV mitigation measures. *J. Wind Eng. Ind. Aerodyn.* **2021**, *208*, 104451. [CrossRef]
8. Wang, J.; Wang, F.; He, R.; Li, J.; Hao, J.; Zhang, J.; Huang, X. Investigation of the intrinsic characteristics of two lock-in regions in a 10:1 π-shaped deck. *Ocean Eng.* **2024**, *293*, 116607. [CrossRef]
9. Zhang, T.; Sun, Y.; Li, M.; Yang, X. Experimental and numerical studies on the vortex-induced vibration of two-box edge girder for cable-stayed bridges. *J. Wind Eng. Ind. Aerodyn.* **2020**, *206*, 104336. [CrossRef]
10. Wu, Y.; Wu, X.; Li, J.; Xin, H.; Sun, Q.; Wang, J. Investigation of vortex-induced vibration of a cable-stayed bridge without backstays based on wind tunnel test. *Eng. Struct.* **2022**, *250*, 113436. [CrossRef]
11. Li, H.-Y.; Xu, Y.-L.; Zhu, L.-D.; Zhang, G.-Q.; Cheng, B.-M. Aerodynamic interference between road vehicles and bridge deck subjected to vortex-induced vibration. *J. Wind Eng. Ind. Aerodyn.* **2024**, *252*, 105845.
12. Larsen, A.; Esdahl, S.; Andersen, J.E.; Vejrum, T. Storebaelt suspension bridge—Vortex shedding excitation and mitigation by guide vanes. *J. Wind. Eng. Ind. Aerodyn.* **2000**, *88*, 283–296. [CrossRef]
13. Laima, S.; Li, H.; Chen, W.; Ou, J. Effects of attachments on aerodynamic characteristics and vortex-induced vibration of twin-box girder. *J. Fluids Struct.* **2018**, *77*, 115–133. [CrossRef]
14. Yuan, W.; Laima, S.; Chen, W.; Li, H.; Hu, H. Investigation on the vortex-and-wake-induced vibration of a separated-box bridge girder. *J. Fluids Struct.* **2017**, *70*, 145–161.
15. Huang, L.; Wang, Q.; Dong, J.H.; Liao, H.L. Vortex-induced vibration mitigation effects of horizontal stabilizers on flat steel box girder with large aspect ratio. *Bridge Constr.* **2022**, *52*, 69–77.
16. Wang, J.; Wang, F.; Xing, F.; Zheng, X.; Li, J.; Zhang, J.; Huang, X. Investigation of two patterns of vortex-induced vibration in a 5:1 rectangular section under different parameters. *Phys. Fluids* **2024**, *36*, 057112. [CrossRef]
17. Li, J.W.; Wu, P.; Hao, J.M.; Pan, H. Experimental and numerical studies on the two "lock-in" regions characteristic of vertical vortex-induced vibration of Π-shaped composite bridge deck. *J. Wind. Eng. Ind. Aerodyn.* **2022**, *228*, 105122. [CrossRef]
18. Zhao, L.; Cui, W.; Shen, X.; Xu, S.; Ding, Y.; Ge, Y. A fast on-site measure-analyze-suppress response to control vortex-induced-vibration of a long-span bridge. *Structures* **2022**, *35*, 192–201. [CrossRef]
19. Hu, C.; Zhao, L.; Guan, X.; Ge, Y. Mitigation mechanism of torsional vortex-induced vibration using aerodynamic countermeasures: Case study on a typical closed-box girder. *Eng. Struct.* **2024**, *318*, 118611. [CrossRef]
20. Xu, F.; Ying, X.; Li, Y.; Zhang, M. Experimental explorations of the torsional vortex-induced vibrations of a bridge deck. *J. Bridge Eng.* **2016**, *21*. [CrossRef]
21. Yang, F.F.; Zheng, S.X.; Yan, Z.X. Vortex-induced vibration and control of split three-box girder bridges. *Struct. Eng. Int.* **2021**, *33*, 7–16. [CrossRef]
22. Chen, X.; Qiu, F.; Tang, H.; Li, Y.; Xu, X. Effects of secondary elements on vortex-induced vibration of a streamlined box girder. *KSCE J. Civ. Eng.* **2020**, *25*, 173–184. [CrossRef]
23. Ge, Y.J.; Zhao, L.; Cao, J.X. Case study of vortex-induced vibration and mitigation mechanism for a long-span suspension bridge. *J. Wind Eng. Ind. Aerodyn.* **2022**, *220*, 104866. [CrossRef]
24. Li, M.; Sun, Y.; Jing, H.; Li, M. Vortex-induced vibration optimization of a wide streamline box girder by wind tunnel test. *KSCE J. Civ. Eng.* **2018**, *22*, 5143–5153. [CrossRef]
25. Hui, Y.; Liu, Z.; Guo, K.; Yang, Q. A Mathematical Model of Nonlinear Aerodynamic Damping for High-Rise Buildings. *J. Eng. Mech. (ASCE)* **2024**, *150*, 04024021. [CrossRef]
26. Hui, Y.; Tang, Y.; Yang, Q.; Chen, B. A Wake-Oscillator Model for predicting VIV of 4-to-1 rectangular section cylinder. *Nonlin. Dyn.* **2024**, *112*, 8985–8999. [CrossRef]
27. Ge, Y.J.; Cao, F.C.; Li, J.W.; Liu, Q.K.; Ma, C.M.; Yang, Y.X.; Zhang, Z.T.; Zhao, L. *Guidelines for Wind Tunnel Testing of Bridges*; Communications Press Co., Ltd.: Beijing, China, 2018.